INFERRING LARGE-SCALE STRUCTURAL CONNECTIVITY FROM LOCAL ACTIVITY IN A MODEL OF THE MOUSE LARGE-SCALE CORTICAL NETWORK

Ronaldo V. Nunes[1], Marcelo Bussotti Reyes[1], Jorge F. Mejias[2], and Raphael Y. de Camargo[1]

[1]Center for Mathematics, Computing and Cognition, Universidade Federal do ABC, São Bernardo do Campo, Brazil

[2]Swammerdam Institute for Life Sciences, University of Amsterdam, Amsterdam, The Netherlands

January 28, 2021

ABSTRACT

Inferring the structural connectivity from electrophysiological measurements is a fundamental challenge in systems neuroscience. Directed functional connectivity measures, such as the Generalized Partial Directed Correlation (GPDC), provide estimates of the causal influence between areas. However, such methods have a limitation because their estimates depend on the number of brain regions simultaneously recorded. We analyzed this problem by evaluating the effectiveness of GPDC to estimate the connectivity of a ground-truth, data-constrained computational model of a large-scale mouse cortical network. The model contains 19 cortical areas modeled using spiking neural populations, and directed weights for long-range projections were obtained from a tract-tracing cortical connectome. We show that the GPDC estimates correlate positively with structural connectivity. Moreover, the correlation

between structural and directed functional connectivity is comparable even when using only a few cortical areas for GPDC estimation, a typical scenario for electrophysiological recordings. Finally, GPDC measures also provided a measure of the flow of information among cortical areas.

1 Introduction

The communication between brain regions is often analyzed through structural and functional connectivity [1]. The former refers to anatomical connections between brain regions generally quantified using tracer injections or diffusion magnetic resonance imaging [2]. The map of these connections is called "connectome" [3], whose analysis includes methods to evaluate the networks defined by nodes (brain regions) and edges (synapses) [4, 5]. Functional connectivity evaluates brain communication from statistical relations between recorded brain signals [6, 1]. Particularly, directed functional connectivity methods use the concept of causality to infer both the intensity and the direction of the connections between brain regions [7]. Even though there is some association between structural and functional connectivity, the relationship between them is not straightforward [1]. While the former is practically static and compose the map of possible pathways for information flow between brain regions, the latter changes continuously and depends, for example, on the dynamical states of brain regions, noise, and strength of structural connections [8].

During electrophysiological procedures, researchers typically record brain signals using electrodes positioned in different depths of brain regions. Even with the improvement in technologies for recording signals, it is usually possible to record signals only from a few areas compared to the number of sources of activity in the brain [9, 10, 11]. Thus, the functional connectivity analysis presents a problem because many regions that may perform as common inputs [7], and influence indirectly other regions [12, 6] are not recorded. Therefore, the comparison between structural and functional connectivity is problematic since spurious inferred causality relations can lead to misinterpretations of electrophysiological data.

Some simulation studies evaluated the relation between directed functional connectivity and structural connections [8, 13, 14, 15]. However, most of these studies used either autoregressive models for the dynamics of each node [16] or rate-based models [13]. These studies provided important steps towards evaluating the reliability of causality measures, but they are still distant from laboratory experimental conditions.

In this work, we investigated the relationship between directed functional connectivity and structural connectivity in a large-scale spiking neuronal network model of the cortex, derived from a cortical connectome of the mouse obtained using tracer injections [17]. Causality measures obtained using GPDC explained most of the variance of structural connection strengths. The mean correlation remained high ($r > 0.6$) even when only a few cortical areas were considered in the GPDC calculation, indicating that this causality measure provides reliable results in typical experimental conditions in which only recordings from a subset of areas are available.

2 Methods

2.1 Neuron model

We modeled the neurons using a single-compartment Hodgkin–Huxley-type model, where the membrane potential of the i-th neuron described by,

$$C_m \frac{dV_i}{dt} = -g_{Na} m_i^3 h_i (V - E_{Na}) - g_K n_i^4 (V - E_k) - g_L (V - E_L) + I_{\text{ext},i} + I_{\text{syn},i}, \qquad (1)$$

the membrane capacitance C_m is 0.50 nF (0.125 nF) for excitatory (inhibitory) neurons. The maximal conductances values were $g_{Na} = 12.5$ μS, $g_K = 4.74$ μS and $g_L = 0.025$ μS. The reversal potentials $E_{Na} = 40$ mV, $E_K = -80$ mV, and $E_L = -65$ mV correspond to the sodium, potassium and leakage channel, respectively [18]. The dynamics of the voltage-gated ion channels are described by activation and inactivation variables m, n, and h, where m and n accounts for the

dynamics of Na channels and h for K channels. The probability that an ion channel is open evolves according to a set of ordinary differential equations [19],

$$\frac{dm}{dt} = \alpha_m(V)(1-m) - \beta_m(V)m, \tag{2}$$

$$\frac{dh}{dt} = \alpha_h(V)(1-h) - \beta_h(V)h, \tag{3}$$

$$\frac{dn}{dt} = \alpha_n(V)(1-m) - \beta_n(V)n, \tag{4}$$

where,

$$\alpha_m(V) = 0.1\frac{(V+16)}{1-\exp(-(V+16)/10)}, \tag{5}$$

$$\beta_m(V) = 4\exp(-(V+41)/18), \tag{6}$$

$$\alpha_h(V) = 0.07\exp(-(V+30)/20), \tag{7}$$

$$\beta_h(V) = [1+\exp(-V/10)]^{-1}, \tag{8}$$

$$\alpha_n(V) = 0.01\frac{(V+20)}{1-\exp(-(V+20)/10)}, \tag{9}$$

$$\beta_h(V) = 0.125\exp(-(V+30)/80), \tag{10}$$

The parameters used in this neuron model was previously reported and applied in some studies that modeled cortical neuronal populations. [20, 19, 21]

2.2 Spiking neuronal population model

Each spiking neuronal population was composed of 2000 neurons, 1600 excitatory and 400 inhibitory. Neurons within each spiking neuronal population were randomly connected with probability $p_{\text{intra}} = 10\%$. The synaptic current I_{syn} that arrives to postsynaptic neuron i is modeled by,

$$I_{\text{syn},i}(t) = \sum_{j \in \text{presyn}} g_{\text{syn},i,j}(t) \left[E_{\text{syn}} - V_i(t)\right], \tag{11}$$

where the index j represent a presynaptic neuron connected to neuron i and the sum over j accounts for all the synapses that impinge on neuron i. E_{syn} is the synaptic reversal potential which is 0 mV for excitatory and -70 mV for inhibitory synapses. The dynamics of synaptic conductance $g_{\text{syn},i,j}$ is described by an exponential function as follows [22],

$$\frac{dg_{\text{syn},i,j}}{dt} = -\frac{g_{\text{syn},i,j}}{\tau}. \tag{12}$$

When a presynaptic neuron j fires a spike, a synaptic weight w is added on the synaptic conductance $g_{\text{syn},i,j}$ after the axonal delay, which was set as 1 ms [19]. The value of w depends on the excitatory/inhibitory nature of the presynaptic and postsynaptic neurons. The synaptic time constant τ is 2 ms and 8 ms for excitatory and inhibitory synapses, respectively. Furthermore, all neurons receive a background input given by a heterogeneous Poisson-process spiking activity with a rate of 7.3 kHz [19]. The effect of the background input in each neuron is an excitatory synaptic current. To add heterogeneity in our model, all synaptic weights w for recurrent connections and background input were taken from a Gaussian distribution (Table 1).

Table 1: **Synaptic weights for intra-areal connections**. Mean synaptic weight $\overline{w}$ and standard deviation σ_w for all possible synapses. E, I, and Input represent excitatory neurons, inhibitory neurons, and external input, respectively. The arrow indicates the direction of the connection.

Synapses	$\overline{w}$ (nS)	σ_w (nS)
$E \rightarrow E$	2.5	1.0
$E \rightarrow I$	2.5	1.0
$I \rightarrow E$	240	10
$I \rightarrow I$	240	10
$Input \rightarrow E$	3.2	1.0
$Input \rightarrow I$	3.2	1.0

2.3 Mouse large-scale cortical network

The mouse cortex's large-scale network model comprises 19 cortical areas where a spiking neuronal population models each area with long-range and recurrent synapses. Parameters related to recurrent synapses were described in the previous session. Neurons from different areas are randomly connected with probability $p_{\text{inter}} = 5\%$. The synaptic weights between cortical areas are based on the recently published anatomical connectivity dataset for the mouse cortex [17] obtained by retrograde tracer injections [23]. This technique consists in injecting a tracer that flows from the target area to the cell bodies, allowing to identify neurons projecting to the target area. The Fraction of Labeled Neurons (FLN) was measured as the ratio of the number of labeled neurons in a source area to the total quantity of labeled neurons in all source areas [24, 25]. The synaptic weights for directed long-range connections are the FLNs scaled by the global scaling parameters $\mu_{\text{E}} = 50$ and $\mu_{\text{I}} = 25$,

$$w^i_{\text{lr,E}} = \mu_{\text{E}} \sum_j^N \text{FLN}_{i,j} \tag{13}$$

$$w^i_{\text{lr,I}} = \mu_{\text{I}} \sum_j^N \text{FLN}_{i,j}. \tag{14}$$

Long-range connections as excitatory, targeting either excitatory or inhibitory neurons with synaptic weight, $w^i_{\text{lr,E}}$, and $w^i_{\text{lr,I}}$, respectively. The index j represents the source area, i the target area, and N is the total number of simulated cortical areas. The axonal delay for long-range connections is given by the ratio between the anatomical distance estimates between cortical areas and the conduction speed set as 3.5 m/s [26].

2.4 LFP signal

We computed the local field potential (LFP) signal as a sum of the currents' absolute values acting upon excitatory neurons in a spiking neuronal population [27, 28]. Thus, for a cortical area in our

model, the LFP signal will be given by,

$$\text{LFP} = R\frac{\sum_i^{N_\text{E}}(|I_{\text{E},i}| + |I_{\text{I},i}| + |I_{\text{bkg},i}|)}{N_\text{E}}, \tag{15}$$

$I_{\text{E},i}$ accounts for both the local (within population) and global (inter-areal projections) excitatory synaptic currents, while $I_{\text{I},i}$ corresponds to the local inhibitory current. $I_{\text{bkg},i}$ is the synaptic current related to the background Poisson input. R represents the resistance of a typical electrode used for extracellular measurements, here chosen to be 1 MΩ [19]. N_E is the number of excitatory neurons in each neuronal population.

The mean was subtracted from the simulated LFP signal. The resultant signal was filtered using a low-pass filter in 1 kHz to avoid aliasing and downsampled to 1 kHz.

2.5 Generalized partial directed coherence

Generalized partial directed coherence (GPDC) is a frequency-domain method of directed functional connectivity established on multivariate vector autoregressive (MVAR) model [29]. Considering that LFP signals from all areas in the model are represented by a set $\mathbf{x}(t) = [x_1(t) \cdots x_N(t)]^T$ of simultaneously observed time series. The MVAR model for $\mathbf{x}(t)$ is defined as:

$$\mathbf{x}(t) = \sum_{k=1}^{p} \mathbf{A}_k \mathbf{x}(t-k) + \epsilon(t) \tag{16}$$

where p is the MVAR model order. $\mathbf{A}_k$ are coefficient matrices in which the element $a_{ij}^{(k)}$ define the effect of $x_j(t-k)$ on $x_i(t)$. The term $\epsilon(t)$ is a vector of N white noises with covariance matrix $\mathbf{\Sigma}$. The GPDC from the time series x_j to the time series x_i at frequency λ is defined as,

$$\text{GPDC}_{ij}(\lambda) = \left| \frac{\frac{1}{\sigma_i}\overline{A}_{ij}(\lambda)}{\sqrt{\sum_{k=1}^{N} \frac{1}{\sigma_k^2}\overline{A}_{kj}(\lambda)\overline{A}_{kj}^*(\lambda)}} \right|^2, \tag{17}$$

where

$$\overline{A}_{ij}(\lambda) = \begin{cases} 1 - \sum_{k=1}^{p} A_{ij,k} e^{-2\pi\sqrt{-1}\lambda k}, & \text{if } i = j \\ - \sum_{k=1}^{p} A_{ij,k} e^{-2\pi\sqrt{-1}\lambda k}, & \text{if } i \neq j, \end{cases} \tag{18}$$

and σ_i^2 refers to the variance of white noise $\epsilon_i(t)$ [29]. λ is a normalized frequency where $\lambda = 0.5$ means one half of the sampling rate fs [30]. The MVAR model was estimated by the method of ordinary least squares (OLS) [31]. Akaike's information criterion gave the model order indicated that the best model order p that was lesser than or equal to 50 [30]. For all analysis it was evaluated the peak of GPDC.

2.6 Weighted FLN and weighted GPDC

In order to investigate the propagation of neuronal activity through the links defined by structural and directed functional connectivity, we defined the weighted FLN (wFLN) and the weighted GPDC (wGPDC) [32],

$$\text{wFLN}_{ij} = \frac{1}{n} \sum_{j=1}^{n} \left(\frac{\text{FLN}_{ij} r_j}{\sum_{j \in S} r_j} \right) \tag{19}$$

$$\text{wGPDC}_{ij} = \frac{1}{n} \sum_{j=1}^{n} \left(\frac{\text{GPDC}_{ij} r_j}{\sum_{j \in S} r_j} \right) \tag{20}$$

where FLN_{ij} is the FLN from area j to area i, r_j is the firing rate for area j, GPDC_{ij} is the peak of GPDC from area j to area i, S is the set of source areas for target area i and finally and n is the cardinatility of set S.

2.7 Numerical simulations

All simulations were performed using the simulator Brian2 [33] applying the exponential Euler method [34] to integrate the differential equations with an integration step of 0.1 ms. Each simulating was 30 s long, generating sufficient data points to apply GPDC on the simulated LFP signals [35].

3 Results

The model of the large-scale cortical network of the mouse is composed of 19 spiking neural populations with recurrent connections and excitatory long-range connections constrained by the directed and weighted structural connectome (Figure 1A and Figure 1B). The dynamical behavior of each simulated cortical area is predominantly asynchronous with transient spike synchronization [36, 37] (Figure 1C). The power spectral density (PSD) of the LFP signal for a cortical area presents a peak in the gamma band (Figure 1D and 1E) [38]. The firing rate of inhibitory neurons is 4.74 ± 0.11, higher than excitatory neurons rate of 3.64 ± 0.42 (Figure 1F). Differences in population behavior are mostly due to inputs from other areas since we sample their parameters from the same distributions (Section 2.2).

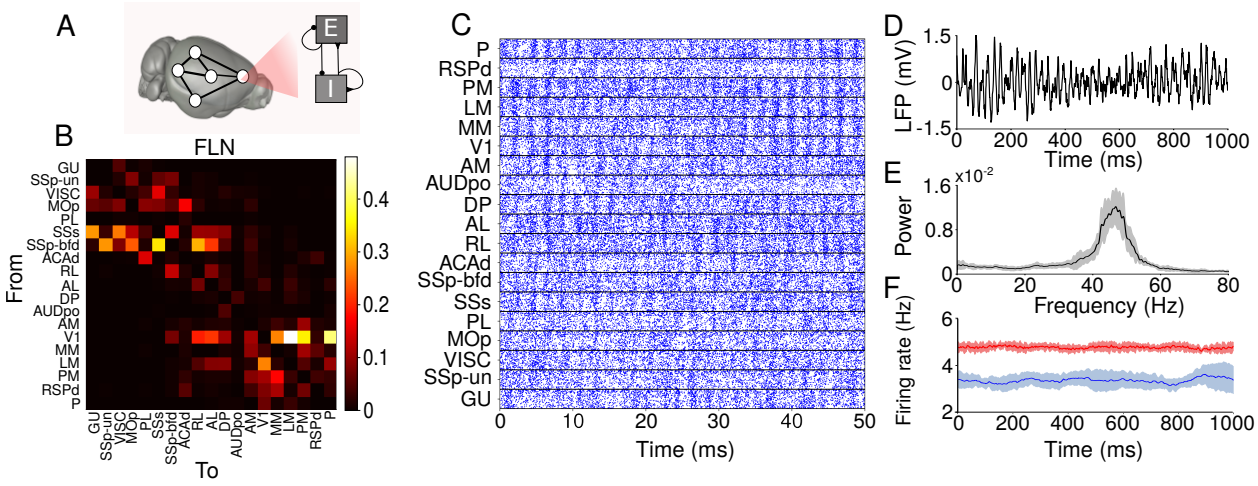

Figure 1: **Large-scale cortical network.** (A) Local neuronal population where E and I are populations of spiking neurons. (B) Map of structural connectivity given by the FLNs. These values define the strength of long-range projections in the large-scale network model. (C) Raster plot of $50ms$ of activity for each cortical area. (D) Simulated LFP signal for an area in the large-scale network model. (E) Power spectral density for simulated LFP signals from one area. Continuous black line corresponds to the average over ten simulations, and the gray shaded area delimits its standard deviation. (F) Firing-rate for excitatory (blue) and inhibitory (red) populations computed using a sliding window of $100ms$. The continuous line corresponds to an average firing-rate over ten simulations, and the shaded area is the standard deviation. To exemplify, we used data from area MOp in (D), (E), and (F).

We first compared the FLN values to the average GPDC over ten simulations of the model. Many medium to strong connections from the structural connectome were also captured by the directed

functional connectivity (Figure 2A and Figure 2B). We used the GPDC largest value (peak), but other approaches such as the average of GPDC over frequencies and area under the GPDC curve (Supplementary Figure S1) produced similar results.

Although the graph density of structural connectome is 97% [17], most structural connections are weak, which leads to a prevalence of weak average GPDC values. Weak structural connections are characteristics shared by connectomes from different mammals, with FLNs varying by several orders of magnitude, log-normally distributed [23, 39, 17, 40]. To evaluate the relation between structural and directed functional connectivity, we plotted GPDC values from ten simulations against FLNs and fit a linear model, obtaining the Pearson correlation r (Figure 2C). The scatter plot presents most points close to the origin due to the predominance of small values for the GPDC and FLN. Interestingly, for some FLNs, there is a high variation of GPDC values over different simulations. The Pearson correlation between FLN and GPDC is 0.73, and GPDC explains approximately 54% of the variance in FLN. This value similar to those obtained by other works that analyzed different structural connectomes using functional connectivity applied to empirical data [41, 42] or firing-rate models [43].

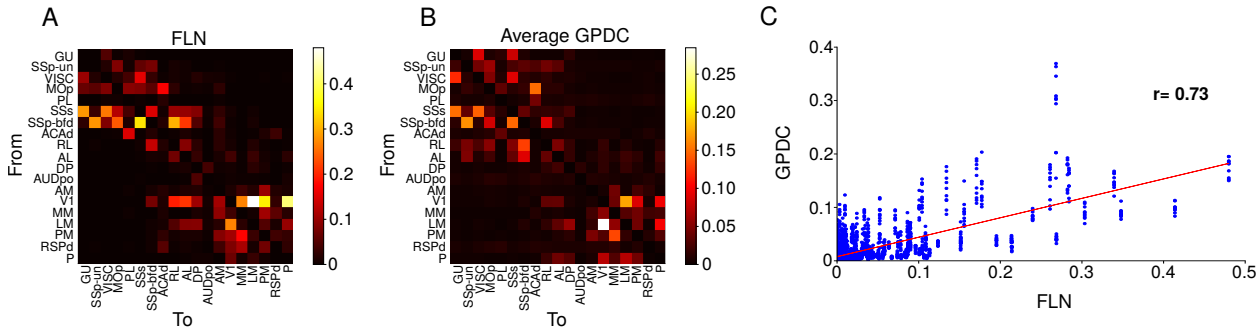

Figure 2: **Relation between structural and directed functional connectivity.** (A) Map of structural connectivity given by the FLNs. (B) Map of directed functional connectivity given by the average of GPDC peaks over ten simulations. (C) Scatter plot of FLNs *versus* GPDC peak. The red line corresponds to the linear fit. The Pearson correlation between FLNs and GPDC is 0.73.

We also investigated the propagation of activity between cortical areas through the pathways defined by structural and directed functional connectivity. The propagation of activity in the cortex is constrained by direct anatomical connections between areas and indirect paths [44], with

the propagation of activity occurring mainly through the strongest long-range projections [24]. The weighted FLNs are strongly correlated to the target areas' firing rate (Figure 3A), while the correlation with the weighted GPDC and firing rate was 0.54 (Figure 3B). This indicates that neural activity propagation is directly dependent on the strength of structural connections and that GPDC can capture part of this activity propagation.

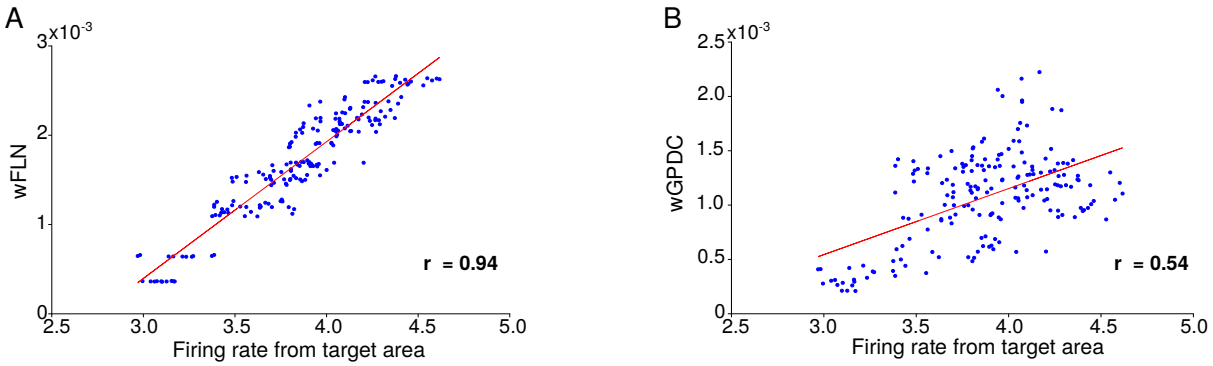

Figure 3: **Propagation of activity through structural and directed functional pathways**. (A) Weighted FLN $versus$ the firing-rate for target areas. The Pearson correlation between Weighed FLNs and firing-rate for target areas is 0.94. (B) Weighted GPDC $versus$ the firing-rate for target areas. The Pearson correlation between Weighed GPDC and firing-rate for target areas is 0.54. Red lines are linear fit.

We analyzed the behavior of GPDC estimates when considering a reduced number of areas, reproducing typical experimental setups. We considered a visual and a frontoparietal cluster, both composed of 7 cortical areas [17]. We evaluated the GPDC estimates between all areas of each cluster (Figures 4C and 4F), conditioned on the whole connectome (Figures 4B and 4E), conditioned on the areas in each cluster, and using only pairwise (bivariate) estimates (Figures 4D and 4G). This analysis simulates the situations where an electrophysiologist only has information from a single cluster of cortical areas or a pair of areas. The highest correlations between the GPDC and FLN occurred when we conditioned GPDC to the whole connectome, followed by GPDC conditioned to the cluster area, and pairwise GPDC. Also, in all cases, the correlation for the frontoparietal cluster was higher in all scenarios.

We extended the analysis to evaluate the effect of cluster size on GPDC correlation to FLN. We used cluster sizes ranging from 2 to 15 areas. We created 150 random clusters sampled from all

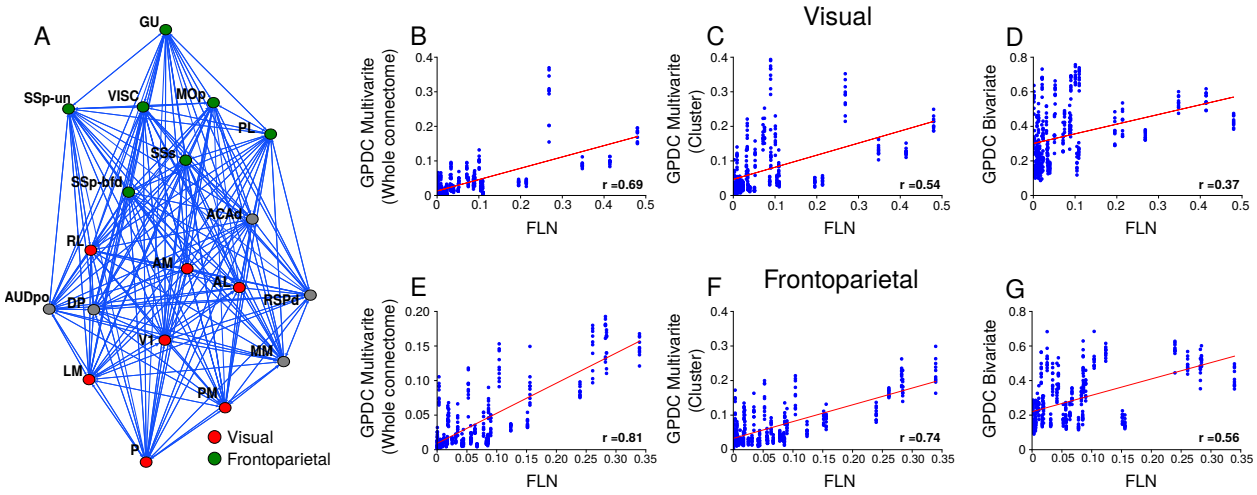

Figure 4: **Correlation between FLN and GPDC for the visual and frontoparietal clusters.** (A) Graph representing the mouse cortical connectome. Nodes represents cortical areas and edges, directed long-range projections between them. Green nodes are cortical areas belonging to the frontoparietal cluster. Red nodes are cortical areas belonging to the visual cluster. Both clusters are composed of 7 cortical areas.(B-D) FLN *versus* GPDC for the visual cluster. The GPDC was computed in (B) conditioned to the whole connectome, (C) conditioned to the areas in the cluster and (D) bivariate approach. (E-G) FLN *versus* GPDC for the frontoparietal cluster. The GPDC was computed in (E) conditioned to the whole connectome, (F) conditioned to the areas in the cluster and (G) bivariate approach. Red lines are linear fit and r is the Pearson correlation.

areas in the connectome for each cluster size and computed the Pearson correlation for (A) the GPDC conditioned on the whole connectome, (B) conditioned on the cluster areas, and (C) pairwise (bivariate). For cases (A) and (B), the Pearson correlation increases, and the standard variation decreases as we increase the cluster size (Figure 5A-B), showing that it is advantageous to include more areas in the GPDC calculation. Surprisingly, the results for scenarios A and B are similar, indicating that using signals measured in a few cortex areas is similar to using signals from the whole cortex, at least regarding the correlation between structural and directed functional connectivity. The correlation between whole connectome GPDC and cluster GPDC estimates increases for large clusters, as expected (Supplementary Figure S2). When considering the bivariate GPDC (Figure 5C), the average Pearson correlation decreases for a range of cluster sizes and remain stable in a low value, which shows that pairwisely estimates of directed functional connectivity are affected by interference from ignored signals.

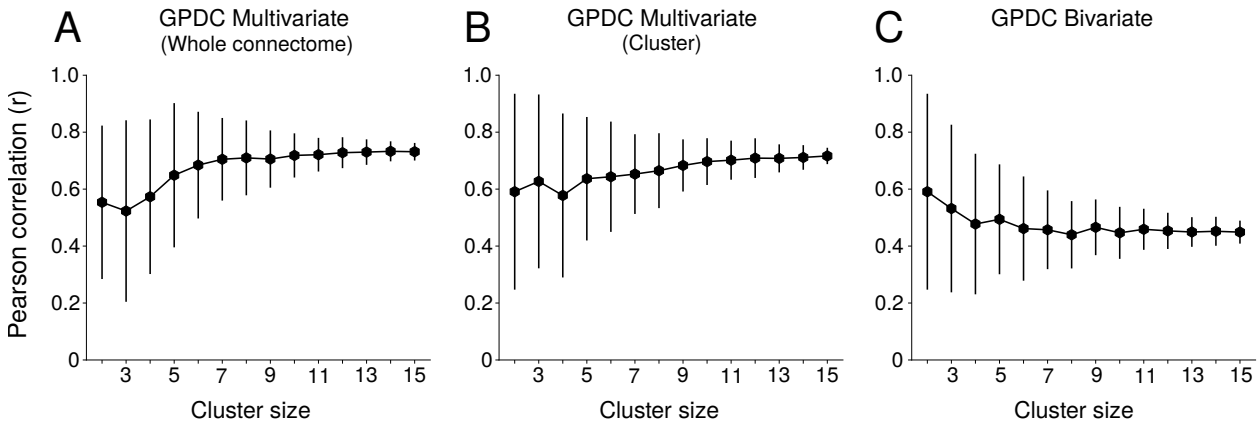

Figure 5: **Correlation between FLN and GPDC for the different cluster size with randomly chosen areas.**. Average (black dots) and standard deviation (error bars) of Pearson correlation for different cluster size. (A) GPDC is conditioned to the whole connectome. (B) GPDC is conditioned only to areas in the cluster. (C) GPDC bivariate.

4 Discussion

We evaluated the inference of directed functional connectivity applying GPDC on simulated LFP signals generated from a large-scale network model for the mouse cortex. Our main result demonstrates that when GPDC is conditioned to a reduced number of areas or the whole connectome, the average Pearson correlation between structural and directed functional connectivity for both cases are comparable. This result provides evidence that it is possible to obtain a reliable relationship between structural and directed functional connectivity in electrophysiological experiments even when signals are recorded from few areas.

Pearson correlation between structural and directed functional connectivity considering the whole connectome and all possible connections in our model is in the range of values obtained in experimental works comparing structural connectivity obtained by tracers and (undirected) functional connectivity [45]. Specifically, previous studies comparing structural and functional connectivity in mice cortex obtained a lower Pearson correlation coefficient than ours [46, 47]. However, besides the undirected functional connectivity adopted in both studies, structural connectivity was set as undirected in one of them (long-range projection weights were given by the average of weights in 2

directions [46]). Also, recordings suffer the influence of the unrecorded source of activities what can affect the relationship between structural and functional connectivity [48].

Although large-scale network models have been used to investigate and predict brain activity observed in electrophysiology and neuroimage [24, 25, 49, 50], as far as we know, the relationship between structural and functional connectivity has been almost unexplored through large-scale network models [51]. Besides, most works in this subject used neural mass description (rate models) to describe each area's activity in the large-scale network model [52, 53]. However, the information propagated between brain regions can be characterized not only by the rate code but also by the temporal code [54, 55, 56, 57, 58]. Additionally, there are hypotheses pointing to spike-timing and spike coherence as essential components of cortical communication [59, 36, 60]. Thus, in our large-scale network model, a spiking neuronal population describes each cortical area's activity [24, 61]. Although spiking neuronal populations are computationally expensive and sometimes prohibitive for large-scale network models simulating many connected brain areas, they present a rich possibility of dynamical behaviors that are not possible using rate models.

The structural connectivity obtained by tracer injections has the advantage that the FLNs between areas are not reciprocal [62], i.e., they are directional. Thus, the best approach to compare structural connectivity and functional connectivity was using a measure that provides the direction of influence from one signal to another. The mouse cortical connectome used in our large-scale network model was obtained through tracer injections [17]. For this reason, GPDC was a suitable choice for evaluating functional connectivity measures. GPDC is a frequency domain measure [29, 30]. However, to have only one value representing the directed functional connectivity, we choose the peak of GPDC, which presented a better correlation with structural connectivity compared to other approaches (Figure S1).

In our results, although the GPDC peak is positively correlated with FLNs, there are several GPDC values that do not correspond to strong FLNs. There are some justifications for these mismatches between GPDC and FLNs. First, in some situations investigated using systems of

few neuronal populations, the direction and weight of directed functional connectivity estimates can be influenced by the phase relation between signals [36, 63, 64]. In large-scale network models, the system's heterogeneity, mainly due to axonal delays for long-range projections, can arise several phase differences between regions [65]. Thus, the relationship between structural and directed functional connectivity can be altered. Second, GPDC classifies the intensity of the connection regarding a signal source [30, 15], what is problematic for comparing with strength of structural connectivity [66]. Therefore, there might be cases where the functional coupling is strong concerning a particular source even though the synaptic projections are not.

The propagation of activity between simulated cortical areas is strongly correlated with weighted FLNs and moderately correlated with weighted GPDC estimates. There are several ways to analyze the propagation of activity in the cortex; some of them can be based only on structural connectivity [44], in amplification caused by changes in projections weights [24] and some based on alterations in firing rates [67]. However, to the best of our knowledge, no studies explore how to acquire signal propagation paths based on directed functional connectivity. Here, we based our analysis on the idea proposed by Cole et al. of activity flow [32]. As we verified in our results, the mean GPDC peak weighted by the firing rate from a source area is positively correlated to the target area's firing rate. Results are better when, instead of considering the GPDC peak, we considered the FLNs. This result suggests that signal propagation pathways are better determined by structural connectivity than by directed functional connectivity. The use of directed functional connectivity to infer signal propagation is not straightforward because several aspects of the model dynamics and some characteristics of the method applied can affect the inference of connections for directed functional connectivity.

The relationship between structural and directed functional connectivity is better when GPDC is conditioned to all areas in the connectome. However, when it is conditioned to few areas in a cluster, structural and directed functional connectivity are moderately correlated. Gămănut et al. identified 6 cluster in the connectome (prefrontal, frontal, parietal, cingulate, temporal and visual) [17] based on the same approach used to investigate the macaque cortex [68]. We joined prefrontal, frontal

and parietal clusters in a single cluster called frontoparietal. The regions AUDpo, and DP, which compose the temporal cluster and ACAd, RSPd, and MM, which belong to the cingulate cluster were excluded from these calculations because they form clusters with small number of regions [17]. The idea was to evaluate the relationship between GPDC and FLNs in specific clusters with the same cluster size. The general results were the same for frontoparietal and visual clusters. For frontoparietal clusters, the range of values for FLN and GPDC is smaller than for visual cluster. The correlation between GPDC and FLN was better in the frontoparietal cluster, where even for the bivariate approach, GPDC and FLNs are moderately correlated.

The correlation between GPDC considering the whole connectome and GPDC considering the cluster increases with the number of areas considered in the measurement (Supplementary Figure S2A). Besides that, the difference between GPDC estimates for those two approaches decreases with the cluster size (Supplementary Figure S2B). It is well known that pairwise estimates of directed functional connectivity present false connections compared to structural connectivity, caused by common input or indirect connections [7, 14, 6]. Novelli et al. showed that the relation between structural and directed functional connectivity in a large-scale network model for the macaque brain is more accurate when the multivariate approach is applied to infer directed functional connectivity than for bivariate approach [52]. Nevertheless, it is uninvestigated the reliability of directed functional connectivity estimates according to the number of areas considered. With our results, we evaluated not only the relationship between structural and directed functional connectivity (Figure 4 and Figure 5) for different cluster sizes but also the directed functional connectivity estimates when a reduced number of areas are considered (Figure S2).

Our large-scale network model has some limitations related to the similarity in different cortical areas' dynamical behavior and the connectome. First, modeled neuronal populations are practically homogeneous excepted by synaptic currents caused by long-range projections. However, in realistic approaches, several biologically based features can be added to the model, for example, cell types, spatial scales, and density of excitatory and inhibitory populations [69, 70, 71]. Second, still related to the homogeneity between cortical areas, the simulated LFP for areas in our large-scale network

model oscillates in gamma band (Figure 1). It is known that the activity of cortical areas in mice can oscillate in different bands [72, 73]. Also, oscillatory activity in the mouse cortex is related to density and type of inhibitory neurons [74, 75]. Recently, it has been shown that the relationship between structural and functional connectivity in the macaque cortex is frequency dependent [76]. Third, it is shown that functional connectivity is dependent on network states [77]. Also, studies in computational neuroscience have been exploring multistability and temporal patterns of functional connectivity [78, 79, 80]. In our model, we did not explore network states and dynamics of directed functional connectivity. The computation of directed functional connectivity is dependent on the data length [35]. Thus, the evaluation of directed functional connectivity patterns in short windows of data can be untrustworthy because of the number of samples considered. Finally, we considered only cortical areas in our large-scale network model. It would be interesting to integrate subcortical areas into the model and verify their impact on the relationship between structural and functional connectivity. Future studies can overcome these limitations by creating more detailed models with biologically plausible neuronal features and connectome composed of cortical and subcortical areas [69, 81].

Our results shed light on the relationship between structural and directed functional connectivity in the circumstances near to those faced by electrophysiologists. We concluded that the reliability of directed functional connectivity estimates and the relationship with structural connectivity relies on the number of areas considered. Despite the limitations of our large-scale network model, our findings can support analysis based on electrophysiological recordings, and our model can be used for other investigations regarding cortical communication.

References

[1] Andrea Avena-Koenigsberger, Bratislav Misic, and Olaf Sporns. Communication dynamics in complex brain networks. *Nature Reviews Neuroscience*, 19(1):17, 2018.

[2] Karen S Ambrosen, Simon F Eskildsen, Max Hinne, Kristine Krug, Henrik Lundell, Mikkel N Schmidt, Marcel AJ van Gerven, Morten Mørup, and Tim B Dyrby. Validation of structural brain connectivity networks: The impact of scanning parameters. *NeuroImage*, 204:116207, 2020.

[3] Olaf Sporns, Giulio Tononi, and Rolf Kötter. The human connectome: a structural description of the human brain. *PLoS Comput Biol*, 1(4):e42, 2005.

[4] Danielle S Bassett, Perry Zurn, and Joshua I Gold. On the nature and use of models in network neuroscience. *Nature Reviews Neuroscience*, 19(9):566–578, 2018.

[5] Danielle S Bassett and Olaf Sporns. Network neuroscience. *Nature neuroscience*, 20(3):353–364, 2017.

[6] Andrew T Reid, Drew B Headley, Ravi D Mill, Ruben Sanchez-Romero, Lucina Q Uddin, Daniele Marinazzo, Daniel J Lurie, Pedro A Valdés-Sosa, Stephen José Hanson, Bharat B Biswal, et al. Advancing functional connectivity research from association to causation. *Nature neuroscience*, 22(11):1751–1760, 2019.

[7] André M Bastos and Jan-Mathijs Schoffelen. A tutorial review of functional connectivity analysis methods and their interpretational pitfalls. *Frontiers in systems neuroscience*, 9:175, 2016.

[8] Ronaldo V Nunes, Marcelo B Reyes, and Raphael Y De Camargo. Evaluation of connectivity estimates using spiking neuronal network models. *Biological cybernetics*, 113(3):309–320, 2019.

[9] Guosong Hong and Charles M Lieber. Novel electrode technologies for neural recordings. *Nature Reviews Neuroscience*, 20(6):330–345, 2019.

[10] Kenneth D Harris, Rodrigo Quian Quiroga, Jeremy Freeman, and Spencer L Smith. Improving data quality in neuronal population recordings. *Nature neuroscience*, 19(9):1165–1174, 2016.

[11] Marieke L Schölvinck, David A Leopold, Matthew J Brookes, and Patrick H Khader. The contribution of electrophysiology to functional connectivity mapping. *Neuroimage*, 80:297–306, 2013.

[12] Ruben Sanchez-Romero and Michael W Cole. Combining multiple functional connectivity methods to improve causal inferences. *Journal of Cognitive Neuroscience*, pages 1–15, 2019.

[13] Xichao Mi, Ning Cheng, and Tao Zhang. Performance comparison between gpdc and pcmi for measuring directionality of neural information flow. *Journal of Neuroscience Methods*, 227:57–64, 2014.

[14] Lionel Barnett and Anil K Seth. The mvgc multivariate granger causality toolbox: a new approach to granger-causal inference. *Journal of neuroscience methods*, 223:50–68, 2014.

[15] Luiz A Baccalá and Koichi Sameshima. Partial directed coherence: a new concept in neural structure determination. *Biological cybernetics*, 84(6):463–474, 2001.

[16] Leonardo Novelli, Patricia Wollstadt, Pedro Mediano, Michael Wibral, and Joseph T Lizier. Large-scale directed network inference with multivariate transfer entropy and hierarchical statistical testing. *Network Neuroscience*, 3(3):827–847, 2019.

[17] Răzvan Gămănuţ, Henry Kennedy, Zoltán Toroczkai, Mária Ercsey-Ravasz, David C Van Essen, Kenneth Knoblauch, and Andreas Burkhalter. The mouse cortical connectome, characterized by an ultra-dense cortical graph, maintains specificity by distinct connectivity profiles. *Neuron*, 97(3):698–715, 2018.

[18] Yoram Gutfreund, I Segev, et al. Subthreshold oscillations and resonant frequency in guinea-pig cortical neurons: physiology and modelling. *The Journal of physiology*, 483(3):621–640, 1995.

[19] Belén Sancristóbal, Raul Vicente, and Jordi Garcia-Ojalvo. Role of frequency mismatch in neuronal communication through coherence. *Journal of computational neuroscience*, 37(2):193–208, 2014.

[20] Alessandro Barardi, Belen Sancristóbal, and Jordi Garcia-Ojalvo. Phase-coherence transitions and communication in the gamma range between delay-coupled neuronal populations. *PLoS computational biology*, 10(7):e1003723, 2014.

[21] Belén De Sancristóbal, Raul Vicente, Jose Maria Sancho, and Jordi Garcia-Ojalvo. Emergent bimodal firing patterns implement different encoding strategies during gamma-band oscillations. *Frontiers in computational neuroscience*, 7:18, 2013.

[22] Petar Tomov, Rodrigo FO Pena, Michael A Zaks, and Antonio C Roque. Sustained oscillations, irregular firing, and chaotic dynamics in hierarchical modular networks with mixtures of electrophysiological cell types. *Frontiers in computational neuroscience*, 8:103, 2014.

[23] Nikola T Markov, MM Ercsey-Ravasz, AR Ribeiro Gomes, Camille Lamy, Loic Magrou, Julien Vezoli, P Misery, A Falchier, R Quilodran, MA Gariel, et al. A weighted and directed interareal connectivity matrix for macaque cerebral cortex. *Cerebral cortex*, 24(1):17–36, 2014.

[24] Madhura R Joglekar, Jorge F Mejias, Guangyu Robert Yang, and Xiao-Jing Wang. Inter-areal balanced amplification enhances signal propagation in a large-scale circuit model of the primate cortex. *Neuron*, 98(1):222–234, 2018.

[25] Jorge F Mejias, John D Murray, Henry Kennedy, and Xiao-Jing Wang. Feedforward and feedback frequency-dependent interactions in a large-scale laminar network of the primate cortex. *Science advances*, 2(11):e1601335, 2016.

[26] Hannah Choi and Stefan Mihalas. Synchronization dependent on spatial structures of a mesoscopic whole-brain network. *PLoS computational biology*, 15(4):e1006978, 2019.

[27] Alberto Mazzoni, Henrik Linden, Hermann Cuntz, Anders Lansner, Stefano Panzeri, and Gaute T Einevoll. Computing the local field potential (lfp) from integrate-and-fire network models. *PLoS computational biology*, 11(12), 2015.

[28] Alberto Mazzoni, Stefano Panzeri, Nikos K Logothetis, and Nicolas Brunel. Encoding of naturalistic stimuli by local field potential spectra in networks of excitatory and inhibitory neurons. *PLoS Comput Biol*, 4(12):e1000239, 2008.

[29] Luiz A Baccala, K Sameshima, and DY Takahashi. Generalized partial directed coherence. In *2007 15th International conference on digital signal processing*, pages 163–166. IEEE, 2007.

[30] Koichi Sameshima and Luiz Antonio Baccala. *Methods in brain connectivity inference through multivariate time series analysis*. CRC press, 2014.

[31] JD Hamilton. Times series analysis, one of princeton university press's notable centenary titles. *Hard over*, 1994.

[32] Michael W Cole, Takuya Ito, Danielle S Bassett, and Douglas H Schultz. Activity flow over resting-state networks shapes cognitive task activations. *Nature neuroscience*, 19(12):1718–1726, 2016.

[33] Marcel Stimberg, Romain Brette, and Dan FM Goodman. Brian 2, an intuitive and efficient neural simulator. *Elife*, 8:e47314, 2019.

[34] James M Bower and David Beeman. *The book of GENESIS: exploring realistic neural models with the GEneral NEural SImulation System*. Springer Science & Business Media, 2012.

[35] Sara Sommariva, Alberto Sorrentino, Michele Piana, Vittorio Pizzella, and Laura Marzetti. A comparative study of the robustness of frequency-domain connectivity measures to finite data length. *Brain topography*, 32(4):675–695, 2019.

[36] Agostina Palmigiano, Theo Geisel, Fred Wolf, and Demian Battaglia. Flexible information routing by transient synchrony. *Nature neuroscience*, 20(7):1014, 2017.

[37] Peter Uhlhaas, Gordon Pipa, Bruss Lima, Lucia Melloni, Sergio Neuenschwander, Danko Nikolić, and Wolf Singer. Neural synchrony in cortical networks: history, concept and current status. *Frontiers in integrative neuroscience*, 3:17, 2009.

[38] György Buzsáki and Xiao-Jing Wang. Mechanisms of gamma oscillations. *Annual review of neuroscience*, 35:203–225, 2012.

[39] Panagiota Theodoni, Piotr Majka, David H Reser, Daniel K Wójcik, Marcello GP Rosa, and Xiao-Jing Wang. Structural attributes and principles of the neocortical connectome in the marmoset monkey. *bioRxiv*, 2020.

[40] György Buzsáki and Kenji Mizuseki. The log-dynamic brain: how skewed distributions affect network operations. *Nature Reviews Neuroscience*, 15(4):264–278, 2014.

[41] Patric Hagmann, Leila Cammoun, Xavier Gigandet, Reto Meuli, Christopher J Honey, Van J Wedeen, and Olaf Sporns. Mapping the structural core of human cerebral cortex. *PLoS Biol*, 6(7):e159, 2008.

[42] Maxwell H Turner, Kevin Mann, and Thomas R Clandinin. The connectome predicts resting state functional connectivity across the drosophila brain. *bioRxiv*, 2020.

[43] Rishidev Chaudhuri, Kenneth Knoblauch, Marie-Alice Gariel, Henry Kennedy, and Xiao-Jing Wang. A large-scale circuit mechanism for hierarchical dynamical processing in the primate cortex. *Neuron*, 88(2):419–431, 2015.

[44] Bertha Vézquez-Rodríguez, Zhen-Qi Liu, Patric Hagmann, and Bratislav Misic. Signal propagation via cortical hierarchies. *Network Neuroscience*, 4(4):1072–1090, 2020.

[45] Milou Straathof, Michel RT Sinke, Rick M Dijkhuizen, and Willem M Otte. A systematic review on the quantitative relationship between structural and functional network connectivity strength in mammalian brains. *Journal of Cerebral Blood Flow & Metabolism*, 39(2):189–209, 2019.

[46] James M Stafford, Benjamin R Jarrett, Oscar Miranda-Dominguez, Brian D Mills, Nicholas Cain, Stefan Mihalas, Garet P Lahvis, K Matthew Lattal, Suzanne H Mitchell, Stephen V David, et al. Large-scale topology and the default mode network in the mouse connectome. *Proceedings of the National Academy of Sciences*, 111(52):18745–18750, 2014.

[47] Joanes Grandjean, Valerio Zerbi, Joshua Henk Balsters, Nicole Wenderoth, and Markus Rudin. Structural basis of large-scale functional connectivity in the mouse. *Journal of Neuroscience*, 37(34):8092–8101, 2017.

[48] Shuixia Guo, Anil K Seth, Keith M Kendrick, Cong Zhou, and Jianfeng Feng. Partial granger causality—eliminating exogenous inputs and latent variables. *Journal of neuroscience methods*, 172(1):79–93, 2008.

[49] Murat Demirtaş, Carles Falcon, Alan Tucholka, Juan Domingo Gispert, José Luis Molinuevo, and Gustavo Deco. A whole-brain computational modeling approach to explain the alterations in resting-state functional connectivity during progression of alzheimer's disease. *NeuroImage: Clinical*, 16:343–354, 2017.

[50] Michael Breakspear. Dynamic models of large-scale brain activity. *Nature neuroscience*, 20(3):340–352, 2017.

[51] Kanika Bansal, Johan Nakuci, and Sarah Feldt Muldoon. Personalized brain network models for assessing structure–function relationships. *Current Opinion in Neurobiology*, 52:42–47, 2018.

[52] Leonardo Novelli and Joseph T Lizier. Inferring network properties from time series using transfer entropy and mutual information: validation of multivariate versus bivariate approaches. *Network Neuroscience*, (Just Accepted):1–52, 2020.

[53] Christopher J Honey, Olaf Sporns, Leila Cammoun, Xavier Gigandet, Jean-Philippe Thiran, Reto Meuli, and Patric Hagmann. Predicting human resting-state functional connectivity from structural connectivity. *Proceedings of the National Academy of Sciences*, 106(6):2035–2040, 2009.

[54] Malte Bieler, Kay Sieben, Nicole Cichon, Sandra Schildt, Brigitte Röder, and Ileana L Hanganu-Opatz. Rate and temporal coding convey multisensory information in primary sensory cortices. *eneuro*, 4(2), 2017.

[55] Anil K Seth. Neural coding: rate and time codes work together. *Current Biology*, 25(3):R110–R113, 2015.

[56] Gerald Hahn, Adrian Ponce-Alvarez, Gustavo Deco, Ad Aertsen, and Arvind Kumar. Portraits of communication in neuronal networks. *Nature Reviews Neuroscience*, 20(2):117–127, 2019.

[57] Arvind Kumar, Stefan Rotter, and Ad Aertsen. Spiking activity propagation in neuronal networks: reconciling different perspectives on neural coding. *Nature reviews neuroscience*, 11(9):615–627, 2010.

[58] Artur Luczak, Bruce L McNaughton, and Kenneth D Harris. Packet-based communication in the cortex. *Nature Reviews Neuroscience*, 16(12):745–755, 2015.

[59] Gerald Hahn, Alejandro F Bujan, Yves Frégnac, Ad Aertsen, and Arvind Kumar. Communication through resonance in spiking neuronal networks. *PLoS computational biology*, 10(8):e1003811, 2014.

[60] Paul HE Tiesinga and Terrence J Sejnowski. Mechanisms for phase shifting in cortical networks and their role in communication through coherence. *Frontiers in human neuroscience*, 4:196, 2010.

[61] Maximilian Schmidt, Rembrandt Bakker, Kelly Shen, Gleb Bezgin, Markus Diesmann, and Sacha Jennifer van Albada. A multi-scale layer-resolved spiking network model of resting-state dynamics in macaque visual cortical areas. *PLoS computational biology*, 14(10):e1006359, 2018.

[62] Xiao-Jing Wang, Ulises Pereira, Marcello GP Rosa, and Henry Kennedy. Brain connectomes come of age. *Current Opinion in Neurobiology*, 65:152–161, 2020.

[63] Fernanda S Matias, Leonardo L Gollo, Pedro V Carelli, Steven L Bressler, Mauro Copelli, and Claudio R Mirasso. Modeling positive granger causality and negative phase lag between cortical areas. *NeuroImage*, 99:411–418, 2014.

[64] Vasily A Vakorin, Bratislav Mišić, Olga Krakovska, Gleb Bezgin, and Anthony R McIntosh. Confounding effects of phase delays on causality estimation. *PLOS one*, 8(1):e53588, 2013.

[65] Spase Petkoski, J Matias Palva, and Viktor K Jirsa. Phase-lags in large scale brain synchronization: Methodological considerations and in-silico analysis. *PLoS computational biology*, 14(7):e1006160, 2018.

[66] Björn Schelter, Jens Timmer, and Michael Eichler. Assessing the strength of directed influences among neural signals using renormalized partial directed coherence. *Journal of neuroscience methods*, 179(1):121–130, 2009.

[67] Navid Hasanzadeh, Mohammadreza Rezaei, Sayan Faraz, Milos R Popovic, and Milad Lankarany. Necessary conditions for reliable propagation of slowly time-varying firing rate. *Frontiers in computational neuroscience*, 14:64, 2020.

[68] Mária Ercsey-Ravasz, Nikola T Markov, Camille Lamy, David C Van Essen, Kenneth Knoblauch, Zoltán Toroczkai, and Henry Kennedy. A predictive network model of cerebral cortical connectivity based on a distance rule. *Neuron*, 80(1):184–197, 2013.

[69] Csaba Erö, Marc-Oliver Gewaltig, Daniel Keller, and Henry Markram. A cell atlas for the mouse brain. *Frontiers in neuroinformatics*, 12:84, 2018.

[70] Quanxin Wang, Song-Lin Ding, Yang Li, Josh Royall, David Feng, Phil Lesnar, Nile Graddis, Maitham Naeemi, Benjamin Facer, Anh Ho, et al. The allen mouse brain common coordinate framework: A 3d reference atlas. *Cell*, 2020.

[71] Daniel Keller, Csaba Erö, and Henry Markram. Cell densities in the mouse brain: a systematic review. *Frontiers in neuroanatomy*, 12:83, 2018.

[72] Tomokazu Tsurugizawa, Boucif Djemai, and Andrew Zalesky. The impact of fasting on resting state brain networks in mice. *Scientific reports*, 9(1):1–12, 2019.

[73] Maxwell A Sherman, Shane Lee, Robert Law, Saskia Haegens, Catherine A Thorn, Matti S Hämäläinen, Christopher I Moore, and Stephanie R Jones. Neural mechanisms of transient neocortical beta rhythms: Converging evidence from humans, computational modeling, monkeys, and mice. *Proceedings of the National Academy of Sciences*, 113(33):E4885–E4894, 2016.

[74] Katerina Kalemaki, Xanthippi Konstantoudaki, Simona Tivodar, Kyriaki Sidiropoulou, and Domna Karagogeos. Mice with decreased number of interneurons exhibit aberrant spontaneous and oscillatory activity in the cortex. *Frontiers in neural circuits*, 12:96, 2018.

[75] Guang Chen, Yuan Zhang, Xiang Li, Xiaochen Zhao, Qian Ye, Yingxi Lin, Huizhong W Tao, Malte J Rasch, and Xiaohui Zhang. Distinct inhibitory circuits orchestrate cortical beta and gamma band oscillations. *Neuron*, 96(6):1403–1418, 2017.

[76] Julien Vezoli, Martin Vinck, Conrado Arturo Bosman, André Moraes Bastos, Christopher Murphy Lewis, Henry Kennedy, and Pascal Fries. The role of anatomical connection strength for interareal communication in macaque cortex. *Available at SSRN 3751057*, 2020.

[77] Iain Stitt, Karl J Hollensteiner, Edgar Galindo-Leon, Florian Pieper, Eva Fiedler, Thomas Stieglitz, Gerhard Engler, Guido Nolte, and Andreas K Engel. Dynamic reconfiguration of cortical functional connectivity across brain states. *Scientific reports*, 7(1):1–14, 2017.

[78] Mathieu Golos, Viktor Jirsa, and Emmanuel Daucé. Multistability in large scale models of brain activity. *PLoS computational biology*, 11(12):e1004644, 2015.

[79] Patricio Orio, Marilyn Gatica, Rubén Herzog, Jean Paul Maidana, Samy Castro, and Kesheng Xu. Chaos versus noise as drivers of multistability in neural networks. *Chaos: An Interdisciplinary Journal of Nonlinear Science*, 28(10):106321, 2018.

[80] Gustavo Deco and Viktor K Jirsa. Ongoing cortical activity at rest: criticality, multistability, and ghost attractors. *Journal of Neuroscience*, 32(10):3366–3375, 2012.

[81] Joseph E Knox, Kameron Decker Harris, Nile Graddis, Jennifer D Whitesell, Hongkui Zeng, Julie A Harris, Eric Shea-Brown, and Stefan Mihalas. High-resolution data-driven model of the mouse connectome. *Network Neuroscience*, 3(1):217–236, 2018.

Supplementary Material

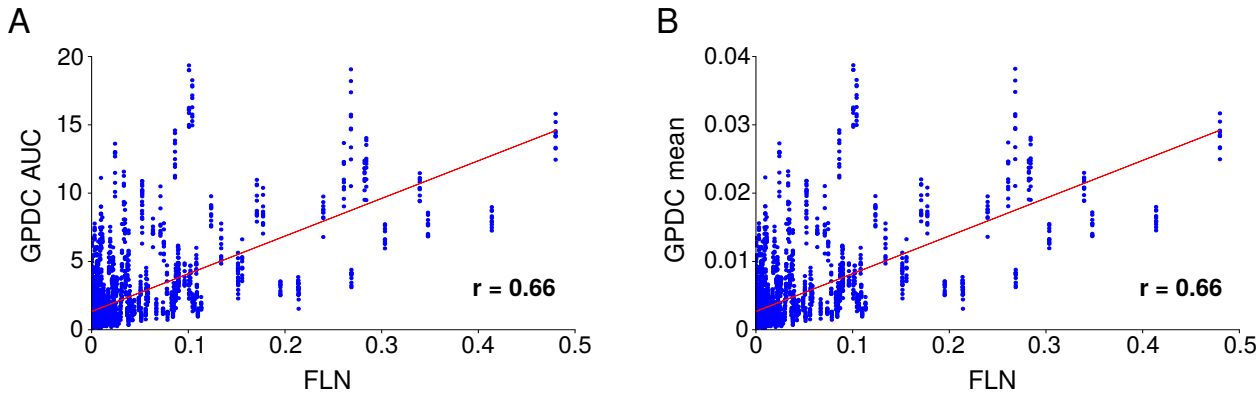

Figure S1: **Area Under Curve (AUC) and mean of GPDC estimates** . (A) GPDC AUC $versus$ FLN. (B) GPDC mean $versus$ FLN. In both cases, the Pearson correlation between GPDC mean or AUC and FLN is 0.66. Red lines are linear fit.

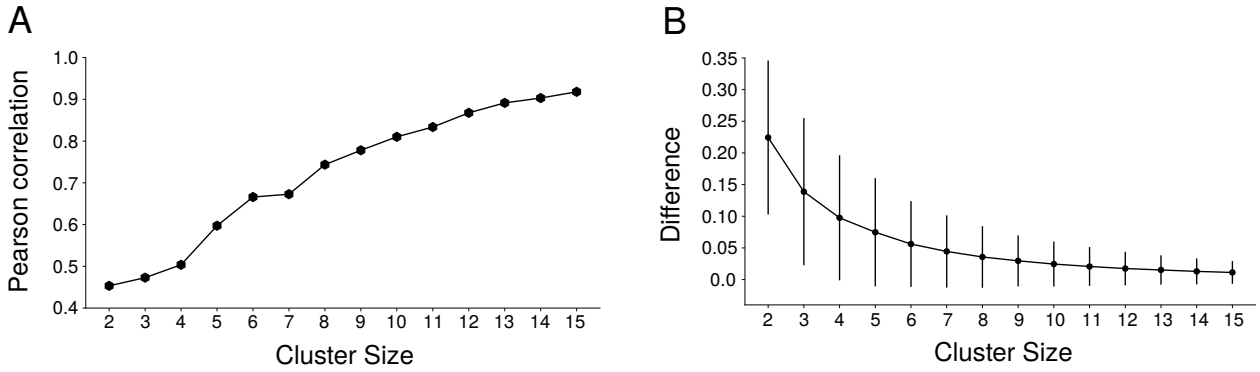

Figure S2: **Correlation and difference between GPDC etimates conditioned to the whole connectome and GPDC estimates conditioned to the cluster areas**. A)Pearson correlation increases with the cluster size. Each bullet represents the average pearson correlation over 150 clusters composed of randomly chosen areas. Comparing all clusters size, the highest value for standard deviation of pearson correlation 0.07. B) Average difference between GPDC estimates conditoned to the whole connnectome and GPDC estimates conditioned to the cluster areas. Average and standard deviation decrease with the cluster size.

Table S1: **Name of areas in mouse cortical connectome.** Adapted from Gămănut et. al., 2018.

Abbreviations	Areas
ACAd	Anterior cingulate area dorsal part
AL	Anterolateral area
AM	Anteromedial area
AUDpo	Auditory cortex posterior area
DP	Dorsal posterior area
GU	Gustatory area
LM	Lateromedial area
MM	Mediomedial area
MOp	Motor cortex primary
P	Posterior area
PL	Prelimbic area
PM	Posteromedial area
RL	Rostrolateral area
RSPd	Rostroplenial area dorsal part
SSp-bfd	Somatosensory cortex primary barrel field
SSp-un	Somatosensory cortex primary unassigned
SSs	Somatosensory cortex secondary
V1	Primary visual area
VISC	Visceral area